The Shadow Positioning Sensors (SPS) for formation flying metrology on-board the ESA-PROBA3 mission

Bemporad, A., Baccani, C., Capobianco, G., Fineschi, S., Focardi, M., et al.

A. Bemporad, C. Baccani, G. Capobianco, S. Fineschi, M. Focardi, F. Landini, D. Loreggia, G. Massone, G. Nicolini, V. Noce, M. Pancrazzi, M. Romoli, S. Buckley, K. O'Neill, E. Renotte, J. S. Servaye, C. Thizy, "The Shadow Positioning Sensors (SPS) for formation flying metrology on-board the ESA-PROBA3 mission," Proc. SPIE 9604, Solar Physics and Space Weather Instrumentation VI, 96040C (21 September 2015); doi: 10.1117/12.2191829

Event: SPIE Optical Engineering + Applications, 2015, San Diego, California, United States

The Shadow Positioning Sensors (SPS) for Formation Flying Metrology on-board the ESA-PROBA3 Mission

A. Bemporad*[a], C. Baccani[b], G. Capobianco[a], S. Fineschi[a], M. Focardi[c], F. Landini[c], D. Loreggia[a], G. Massone[a], G. Nicolini[a], V. Noce[c], M. Pancrazzi[c], M. Romoli[b], S. Buckley[d], K. O'Neill[d], E. Renotte[e], J. S. Servaye[e], C.Thizy[e]

[a]INAF - Turin Astrophysical Observatory, Via Osservatorio 20, 10025 Pino Torinese - Italy;
[b]University of Florence - Dept. of Physics and Astronomy, Largo E. Fermi 2, 50125 Firenze - Italy;
[c]INAF - Arcetri Astrophysical Observatory, Largo E. Fermi 5, 50125 Firenze - Italy;
[d]Sensl, 6800 Airport Business Park, Cork - Ireland;
[e]CSL - Centre Spatial de Liège, Liège Science Park, 4031 Angleur (Liège) - Belgium.

ABSTRACT

PROBA3 is an ESA technology mission devoted to in-orbit demonstration of the formation flight (FF) technique, with two satellites kept at an average inter-distance by about 144 m. The ASPIIC instrument on-board PROBA3 will be the first ever space-based coronagraph working on one satellite and having the external occulter located on the second satellite, thus allowing observations of the inner solar corona with unprecedented reduction of stray light. During the observational periods, the FF configuration will be maintained with very high precision and two different techniques will be implemented: the use of Shadow Positioning Sensors (SPS) located on the Coronagraph Spacecraft (diodes measuring the penumbral light intensity on the entrance pupil plane) and the use of Occulter Position Sensor LEDs (OPSE) located on the back side of the Occulter Spacecraft. This paper will review the main instrumental requirements on the SPS needed to determine the 3-dimensional relative positioning of the two PROBA3 satellites with high precision.

Keywords: Solar Corona, Coronagraph, Formation Flight, In-Orbit Demonstration (IOD), Global Navigation System (GNS), Satellite attitude control.

1 INTRODUCTION

The PROBA3 mission has been conceived by ESA to in-orbit demonstrate, with the required accuracy, the formation flying (FF) techniques and technologies to be adopted on-board the next generation of FF satellites. FF (not to be confused with Rendezvous and spacecraft constellations/trains) is the operational technique by which separate spacecraft maintain a predefined geometry with high accuracy so that they can be considered as a single virtual satellite. In particular, PROBA3 shall carry a 150m length Coronagraph ASPIICS (*Association of Spacecraft for Polarimetric and Imaging Investigation of the Corona of the Sun*) [1][2] split on two spacecraft to be maintained in FF configuration: the Coronagraph Spacecraft (CSC) and the Occulter Spacecraft (OSC).

The ISD (inter-satellite distance) is defined as:

$$\mathrm{ISD} = (R_D - r_p) / \tan(1.02\, R_{Sdeg})$$

where R_D is the in-flight disk radius (occulter diameter), r_p is the pupil radius, R_{Sdeg} is the apparent radius of the Sun (in radians) variable according to Earth-Sun distance variation and position of the orbit apogee with respect to the Sun direction. In particular, the occulter radius is R_D = 71 cm and the pupil radius is r_p = 2.5 cm, hence given the Earth-Sun distances r_{ES} at perihelion ($r_{ES} = 147.166462 \cdot 10^6$ km) and aphelion ($r_{ES} = 152.171522 \cdot 10^6$ km) the parameter ISD will have a maximum value $\mathrm{ISD}_{\max}$ = 146.935 m and $\mathrm{ISD}_{\min}$ = 142.101 m. The ISD variation will allow to have during

Solar Physics and Space Weather Instrumentation VI, edited by Silvano Fineschi, Judy Fennelly, Proc. of SPIE Vol. 9604, 96040C · © 2015 SPIE
CCC code: 0277-786X/15/$18 · doi: 10.1117/12.2191829

different phases of the mission the same size of the umbral region projected on the entrance pupil plane R_{shad}, which is given by

$$R_{shad} = 71 \text{ cm} - \text{ISD}\cdot\tan(\vartheta) = 71 \text{ cm} - \text{ISD}\cdot\tan(R_{sun} / r_{ES}) = 38.43 \text{ mm} \sim 38.5 \text{ mm}.$$

We point out here that, according to the above numbers, the geometrical configuration while the two spacecraft are in FF configuration for an average ISD = 144 m can be qualitatively described as shown in Figure 1.

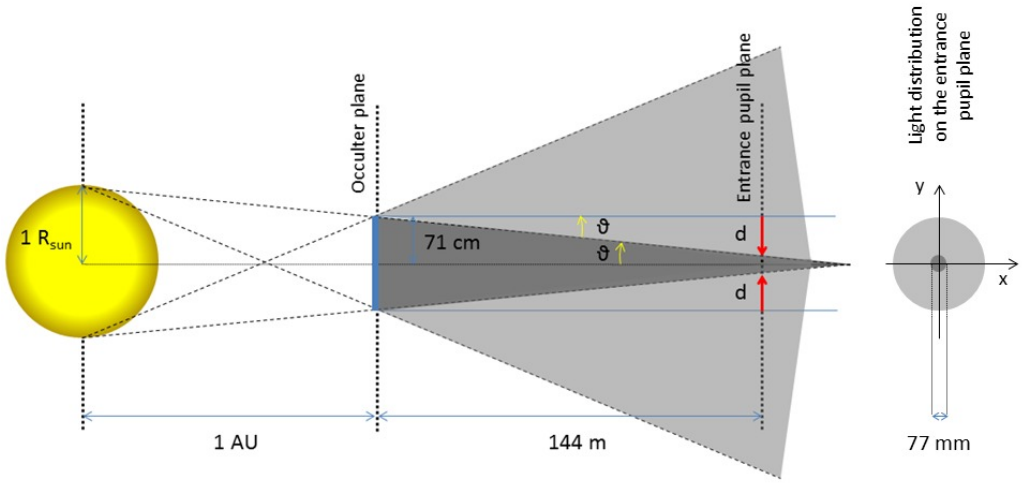

Figure 1: the geometrical volumes interested by a penumbral (light gray) and umbra (dark gray) lights (left panel), and the corresponding distribution of umbra and penumbral lights projected over the entrance pupil plane (right panel).

If we indicate in general with r_{SPS} the radius of the circumference where the SPS are located on the entrance pupil plane, a first SPS will fall in the umbral region for lateral displacements larger than r_{SPS} – 38.5 mm. Given the radius of the shadow R_{shad} and the assumed SPS circumference radius r_{SPS}, the tangential displacement needed to have two SPS falling in the umbra at the same time has been computed as the shift needed to have an interception between the SPS circumference and the shadow circumference shifted in the direction of the bisector of the X and Y axes. This shift corresponds to

$$d = \frac{1}{2}\left(r_{SPS} \pm \sqrt{2R_{shad}^2 - r_{SPS}^2}\right).$$

The above formula also provides the minimum r_{SPS} value required in order to avoid the situation when 2 SPS will fall at the same time in the umbra, which is given by the condition

$$2R_{shad}^2 - r_{SPS}^2 < 0 \quad \rightarrow \quad r_{SPS} > \sqrt{2}\, R_{shad}\,.$$

Hence, with R_{shad} = 38.5 mm the minimum radius of the SPS circumference to avoid the situation described above will be ~ 54.4 mm. For this reason, taking also into account other physical construction limits in the Coronagraph Optical Box (COB), the 8 SPS sensors will be placed on a circumference centered on the optical axis with radius r_{SPS} = 55 mm, separated by the same relative angular distance by 45°, as it is shown in Figure 2.

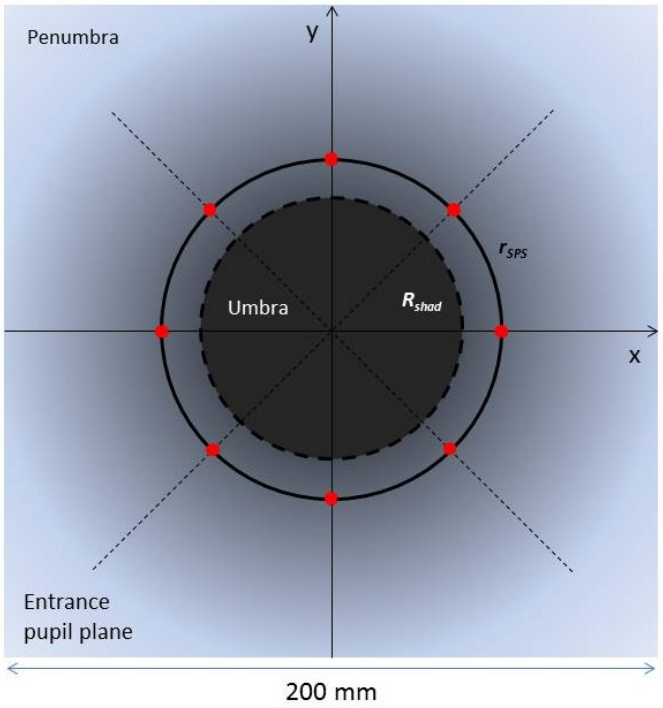

Figure 2: locations of the 8 SPS (Shadow Positioning Sensors, red filled circles) for PROBA-3 on the Coronagraph entrance pupil plane with respect to the umbra and penumbra regions (see text).

The FF configuration will be maintained at high precision with two different metrological sensors: the Shadow Positioning Sensors (SPS) and the Occulter Position Sensor Emitter (OPSE). A description of the metrology based on the OPSE system can be found in [3]; in this paper we will focus only on the metrology based on SPS measurements. In particular: a system of 8 SPS will be located on the CSC to measure the intensity of the penumbral light generated by the OSC. By measuring the penumbra illumination level at 8 different points located on the entrance pupil plane of the Coronagraph, the SPS will provide an absolute measurement of the FF configuration. In particular, the mission SPS performance and goal requirements are listed below.

1. Performance requirement: the Shadow Position Sensor (SPS) shall be used to verify that the Coronagraph Instrument's entrance pupil is centred within the umbra cone of the Occulter Disk. At the ISD specified in COR-IIDA-1011 and within +/- 10mm of the ideal position in lateral and +/- 100mm in range, the SPS shall have a lateral measurement accuracy of 50μm (3-σ) in each axis, and a longitudinal measurement accuracy of 1 mm (3- σ). These accuracies are with respect to the axis connecting the centre of the Occulter with the centre of the Sun.
2. Performance goal: the SPS should be able to return a 3D relative position measurement at reduced performance within a range of +/- 50mm in lateral and +/- 500mm in longitudinal (i.e. the SPS should always return a 3D measurement within a box of 100mm in width and height and 1000mm in depth, centered on the ideal position).
3. SPS SPFT: the SPS design shall not contain any single point of failure.

The determination of an algorithm providing the displacement of the occulter spacecraft with respect to the coronagraph spacecraft for the PROBA-3 mission given the measured level of illumination by the SPS in the penumbra requires many different steps, described in this paper. Every point (x, y) in the penumbral region lying over the entrance pupil plane is characterized by a level of illumination related to the fraction of the solar disk "seen" by the considered point, going from no illumination for the points located in the umbra (where there is no visible fraction of the solar disk) up to total illumination for the points located out of the penumbra (where the whole solar disk is visible). For all the intermediate points located in the penumbra the amount of light impinging on the SPS sensors can be computed geometrically by estimating the fraction of the solar disk "seen" by each point. As described below, the shape of solar disk projected on

the plane where the occulter should be in the ideal case can be well approximated with a circle, while the occulter will be described by an ellipse in order to also take into account possible occulter tilt angles.

As it will be shown below, the level of illumination is also dependent on two other effects: the limb darkening effect and the presence of sunspots close to the limb. This can be understood as follows: the SPS detectors are located very close to the edge of the umbra region and the corresponding amount of light they collect is due to emission coming from a thin "crescent-shaped" fraction of the solar disk emerging behind the occulter. This fraction of the disk is for the majority located at the solar limb, where the emission is reduced by a factor of about ~ 2.7 [4] with respect to the emission coming from the center of the disk because of the limb darkening effect. Hence, the level of illumination estimated in the penumbra by assuming uniform distribution of solar radiation on the disk is significantly overestimated. Moreover, when a sunspot group will be located at the limb, this will correspond to a further reduction in the illumination in the penumbra for all the points located in the entrance pupil plane "seeing" emission coming from the "crescent-shaped" fraction of the solar disk where the sunspots are located. Because the photospheric emission coming from sunspots is reduced, respectively, down to 5-25% and 65-85% of the quiet sun photospheric light in the sunspot umbra and penumbra [5], this will provide a further reduction in the SPS illumination depending mainly on the sunspot size and location. The first effect can be easily included in the requested algorithm, while the second effect cannot be included in the algorithm because it is not possible to forecast at any time the transit of a sunspot at the limb.

We notice here that the above two effects (limb darkening and sunspots) have not been taken into account in any of the previous simulations [6][7][8] of the penumbra illumination profile for the PROBA-3 mission. Nevertheless, as we are going to show here, the inclusion of these effects is mandatory in order to reproduce the real penumbra illumination level with the precision by ~0.5% required to perform the FF metrology for PROBA-3. This paper is organized as follows: after the present introduction (1), we describe how the penumbra illumination profile has been derived (2). The resulting illumination profile has then been used to estimate the expected output currents from SPS (3); further corrections due to other effects not taken into account are then described (4),as well as two numerical test we performed to verify the effect of sunspots and the correctness of the derived penumbra illumination curve (5). We conclude providing the SPS required sensitivities on the penumbra illumination measurements (6) and providing a preliminary version of the SPS algorithm to be used on-board for the absolute measurements of FF metrology (7). All the results are then summarized in the last paragraph (8).

2 FRACTION OF SOLAR DISK SOURCE OF PENUMBRAL LIGHT

The amount of light coming from the solar disk and impinging on a single SPS detector (assumed to have no physical extension here) corresponds to the geometrical area of the fraction of the solar disk not covered by the occulter as seen by the SPS (shown in Figure 3). By assuming that the solar disk has a circular shape (which is an acceptable approximation, see below) and that the occulter edge has the projected shape of an ellipse (true for the general case of a circular occulter with a given tilt angle) a derivation of this area requires as a first step the determination of the intersection points between a circle and an ellipse.

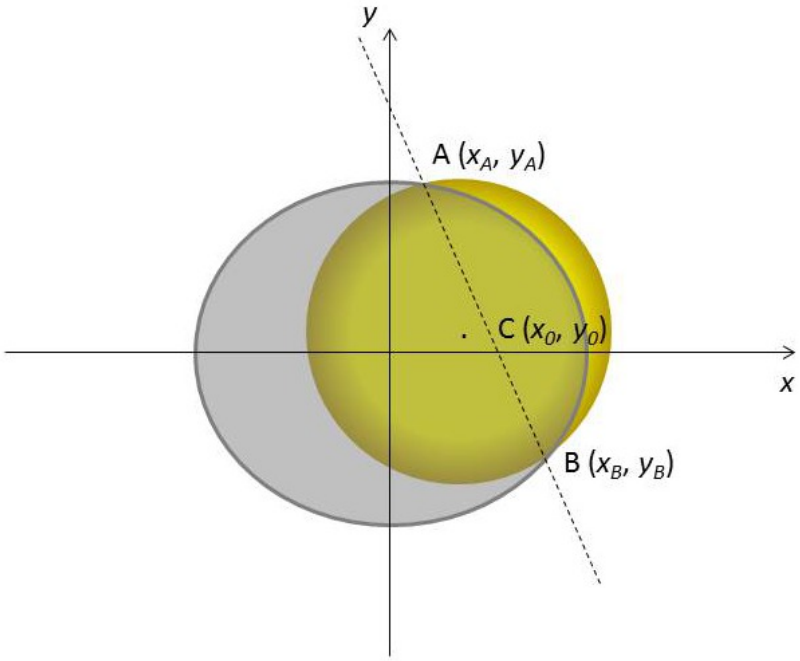

Figure 3: cartoon showing the general geometrical configuration defining the location of the solar disk (yellow filled circle) and the fraction of the disk emerging behind the occulter (gray filled ellipse).

Let's assume for simplicity that the ellipse representing the occulter is centered on the origin of the reference frame with symmetry axes parallel to the main axes of the reference system, while the circle representing the solar disk is shifted with center in the position C (x_0, y_0), as shown in Figure 3, hence the intersection points are given by

$$\begin{cases} \dfrac{x^2}{a^2} + \dfrac{y^2}{b^2} = 1 \\ (x - x_0)^2 + (y - y_0)^2 = R^2 \end{cases}$$

A general solution to this system of equations is given by the following fourth order polynomial:

$$A^2 y^4 + 2AB y^3 + \left(B^2 + 2AC + a^2/b^2\right) y^2 + 2BC y + C^2 - a^2 = 0$$

where

$$A = \frac{1}{2x_0}\left(1 - \frac{a^2}{b^2}\right); \quad B = -\frac{y_0}{x_0}; \quad C = \frac{x_0^2 + y_0^2 - R^2 + a^2}{2x_0}$$

The 4 possible roots of the above 4-th order polynomial, once it is rewritten in the usual form

$$\alpha y^4 + \beta y^3 + \gamma y^2 + \delta y + \varepsilon = 0$$

are given by

$$y_{1,2} = -\frac{\beta}{2\alpha} - S \pm \frac{1}{2}\sqrt{\frac{q}{S} - 4S^2 - 2p}; \quad y_{3,4} = -\frac{\beta}{2\alpha} + S \pm \frac{1}{2}\sqrt{-\frac{q}{S} - 4S^2 - 2p}$$

where

$$p = \frac{8\alpha\gamma - 3\beta^2}{8\alpha^2}; \quad q = \frac{\beta^3 - 4\alpha\beta\gamma + 8\alpha^2\delta}{8\alpha^3}$$

and

$$S = \frac{1}{2}\sqrt{-\frac{2}{3}p + \frac{1}{3\alpha}\left(Q + \frac{\Delta_0}{Q}\right)}; \quad Q = \sqrt[3]{\frac{\Delta_1 + \sqrt{\Delta_1^2 - 4\Delta_0^3}}{2}}$$

$$\Delta_0 = \gamma^2 - 3\beta\delta + 12\alpha\varepsilon$$

$$\Delta_1 = 2\gamma^3 - 9\beta\gamma\delta + 27\beta^2\varepsilon + 27\alpha\delta^2 - 72\alpha\gamma\varepsilon$$

In general up to 4 points of intersections between the ellipse and the circle can be found. Nevertheless, for the expected relatively small values of the occulter tilt angle and shift with respect to the solar disk, these points of intersection are usually not more than 2. In any case, the determination of the coordinate of these two points requires the solution of the above 4-th order polynomial. All the special cases occurring when $x_0 = 0$ or $y_0 = 0$ or $a = b$ or other cases need to be analysed separately.

Given the two roots for the y coordinates of the 2 intersection points, obviously the corresponding x coordinates are found by replacing them into the equation of the circle and of the ellipse and imposing that the coordinate of that point satisfy the equations of both curves. In what follows let's call these two points A and B.

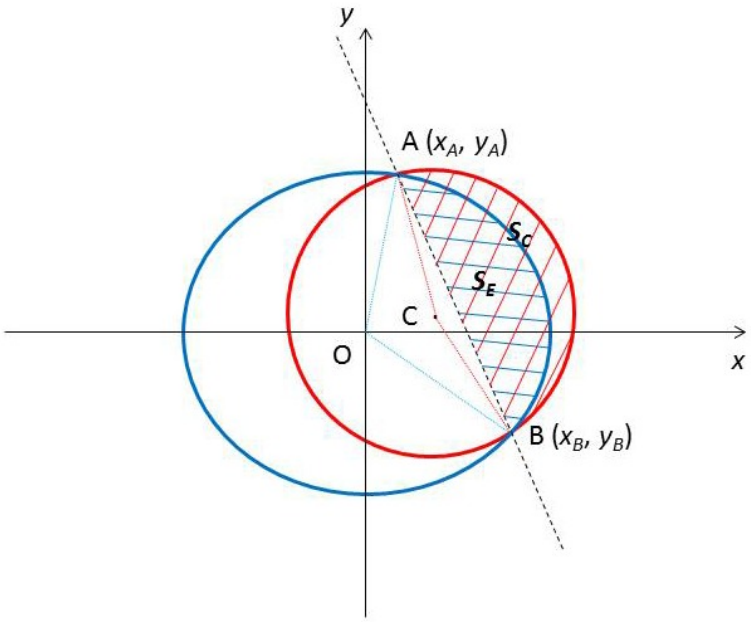

Figure 4: location of the circular and elliptical segments (S_C and S_E, respectively) defined by the intersection points A and B between the circle and the ellipse.

Now we assume that the coordinates of these two points A (x_A, y_A) and B (x_B, y_B) have been determined as described above and also that the distance between the origin and the circle's center C (x_0, y_0) is smaller than the distance between the origin and the straight line passing through A and B. This second condition is usually satisfied for the small shift of the circle expected. In this case the area H of the solar disk (i.e. the circle) emerging behind the occulter (i.e. the ellipse) is given by

$$H = S_C - S_E$$

where S_C is the area of the minor circular segment bounded by the cord AB and the circle (see Figure 4, red shaded area), while S_E is the area of the minor elliptical segment bounded by the cord AB and the ellipse (see Figure 4, blue shaded area). Hence, determination of H requires a determination of S_C and S_E. Now if

$$\overline{AB} = \sqrt{\left(x_B - x_A\right)^2 + \left(y_B - y_A\right)^2} \; ; \quad d = \frac{\left|y_0 - mx_0 - q\right|}{\sqrt{1+m^2}}$$

are, respectively, the length of the AB segment and its distance from the circle center (x_0, y_0), with m and q usual coefficients of the equation of the straight line passing through A and B, then it is easy to show that

$$S_C = \vartheta R^2 - \frac{1}{2}\overline{AB}\, d$$

where θ = arctan[AB/(2d)]; hence S_C is given by the difference between the area of the circular sector and the area of the triangle ACB.

On the other hand the area of the elliptical segment is given by the difference between the area of the elliptical sector and the area of the triangle AOB, and then is given by

$$S_E = F\left(\vartheta_1\right) - F\left(\vartheta_0\right) - \frac{1}{2}\left|x_A y_B - x_B y_A\right|$$

where

$$F\left(\vartheta\right) = \frac{ab}{2}\left\{\vartheta - \arctan\left[\frac{\left(b-a\right)\sin 2\vartheta}{\left(b+a\right)+\left(b-a\right)\cos 2\vartheta}\right]\right\}$$

with θ = angle between the x-axis and the vector going from the origin to the considered point (positive when measured counter-clockwise, see Figure 5 for definition of function F).

The above procedure gives all the formulas required to compute the area H of the solar disk emerging from the occulter, under the assumption that these can be geometrically represented by a circle and an ellipse, respectively. In reality, the solar disk is not a perfect circle: the radius at the poles is smaller by about 6 km than the radius at the equator, which corresponds to a difference by about 8.27 m arcsec as seen from the distance of 1 AU. The minimum occulter displacement Δs (in the x or y directions) to be detected is Δs = 50 μm for an occulter located at a distance by 144 m from the coronagraph, and this corresponds to an angle by 71.6 m arcsec. Hence, the minimum displacement angle to be detected is about 9 times larger than the oblateness of the solar disk, that can be considered with a circular shape.

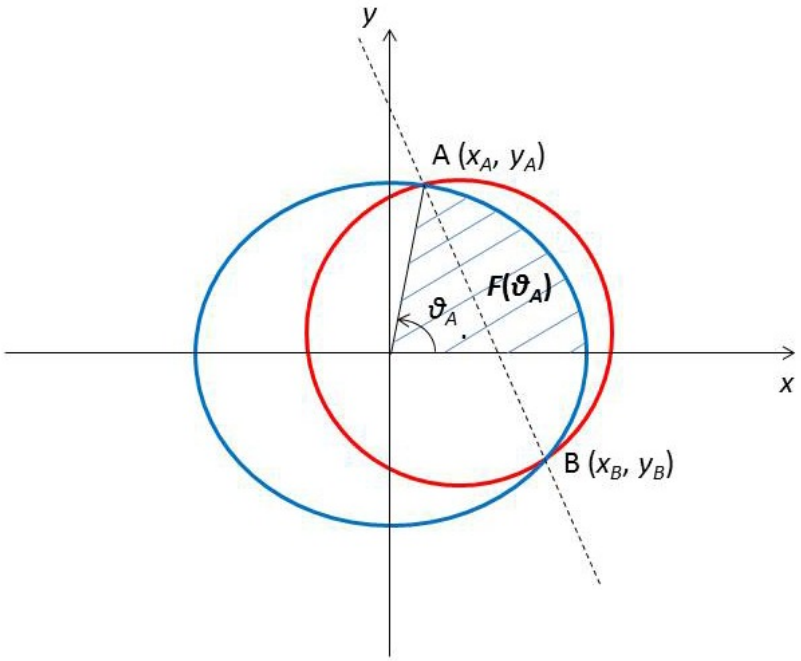

Figure 5: determination of the elliptical sector area.

On the other hand, the projected shape of the occulter needs to be described as an ellipse: for instance with a tilt angle of 0.5° around the *x*-axis, the occulter radius in the *y* direction will be reduced by a factor cos(0.5°) ~ 0.99996192, and this will correspond to an ellipse with eccentricity $e = (1 - a^2/b^2)^{1/2} \sim 0.008727$.

Overall, the above procedure is valid only under the simplifying hypothesis that the solar disk is a uniform source of radiation, but this is not true in the more general case because at least of the presence of:

1. limb darkening (qualitatively shown in Figure 1),
2. sunspot groups possibly located close to the limb.

Hence, in general, computation of the area *H* is not the final solution to the problem: this area needs to be integrated over the variable function of the limb darkening that provides the disk brightness as a function of the angle ϑ between the considered point on the disk and the line of sight. This function is given by

$$I_\lambda(\theta)/I_{\lambda 0} = 1 - u_\lambda - v_\lambda + u_\lambda \cos\theta + v_\lambda \cos^2\theta$$

where $I_{\lambda 0}$ is the disk intensity at wavelength λ at the disk center, $I_\lambda(\vartheta)$ is the disk intensity at wavelength λ at an angle ϑ from the disk center, and u_λ and v_λ are limb darkening coefficients depending on the considered wavelength bandpass (see below).

3 ESTIMATE OF THE SPS OUTPUT CURRENTS

3.1 Description of the computation

The solar flux or spectral irradiance F_λ [W m^{-2} nm^{-1}] (shown in Figure 6 together with the SPS responsivity [A/W]) is computed by integrating the contributions from the entire solar disk: the average disk intensity I_a [W m^{-2} sr^{-1} nm^{-1}] times the area of the solar disk A_s (m^2) gives the total amount of radiation emitted by the Sun towards the collecting surface A_c. Hence, the radiative flux F_λ (corresponding to the radiative energy per unit area and unit wavelength, measured in W m^{-2} nm^{-1}) crossing the collecting surface is given by

$$F_\lambda = \frac{1}{A_c}\left(I_a A_s \frac{A_c}{D^2}\right) = I_a \Omega_s$$

where $\Omega_s = A_s / D^2 = 6.79994 \cdot 10^{-5}$ sr and A_c / D^2 are the solid angles subtended by the solar disk and by the collecting surface, respectively, at the distance D = 1 AU.

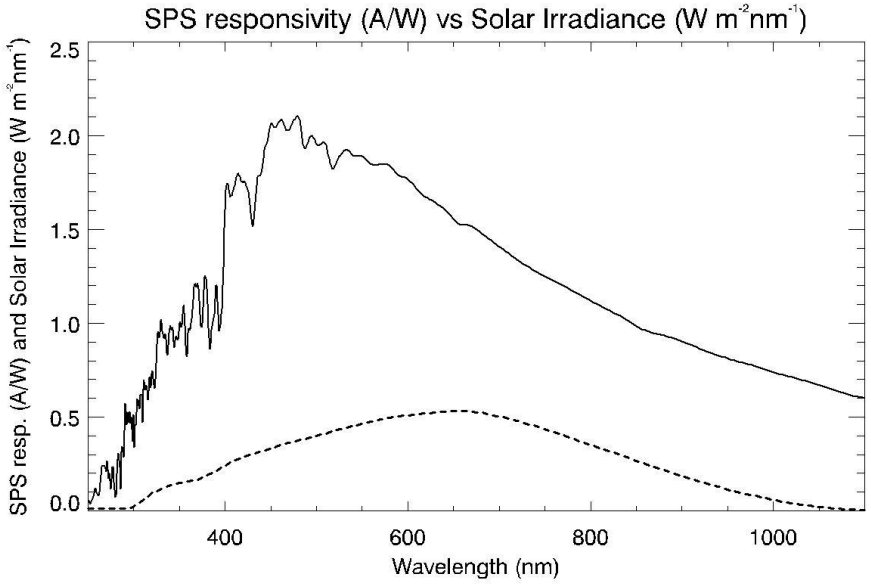

Figure 6: the solar spectral irradiance (solid line, [W m^{-2} nm^{-1}]) and the SPS responsivity curve (dashed line, [A/W]).

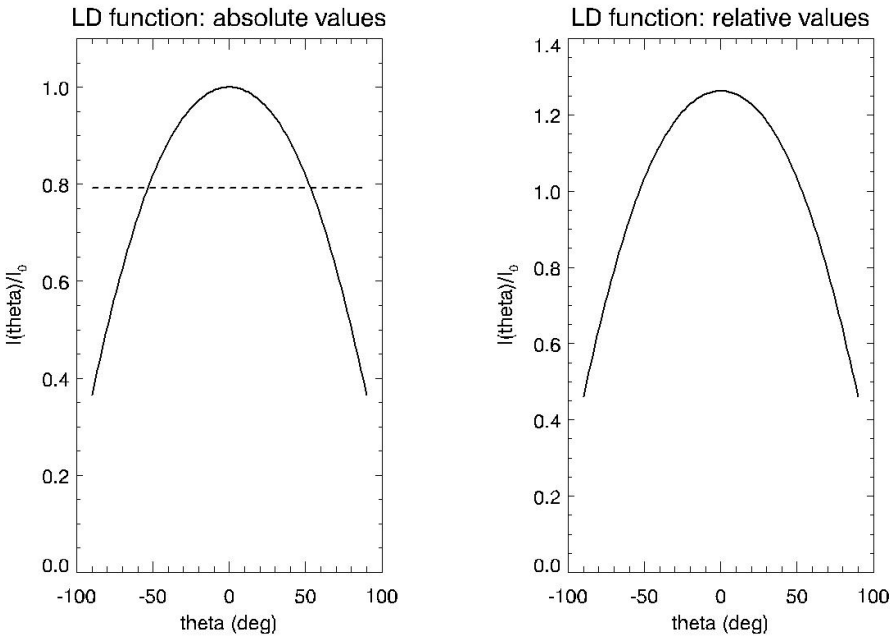

Figure 7, left: absolute values of the limb darkening (LD) function across the disk (solid line) and the average value of the same function over the whole disk (dashed line). Right: variations of LD function relative to the average value shown on the left plot.

Nevertheless, in general the radiation emitted by the solar disk is not uniform, because of well known center-to-limb variations resulting in a limb darkening in the visible range and limb brightening in the EUV range. If θ is the angle between the vector connecting the Sun center with the considered point on the disk and the line of sight, the limb darkening function is given by

$$\frac{I_\lambda(\vartheta)}{I_{\lambda 0}} = 1 - u_\lambda - v_\lambda + u\cos\vartheta + v\cos^2\vartheta$$

where u_λ and v_λ are the (wavelength dependent) limb darkening coefficients (adimensional) and $I_{\lambda 0}$ [W m^{-2} sr^{-1} nm^{-1}] is the intensity at the center of the solar disk. This is related to the average disk intensity defined above by

$$I_a = \frac{1}{\Omega_s}\int_{\Omega_s} I_\lambda(\vartheta)\,d\omega \quad \leftrightarrow \quad F_\lambda = I_a\Omega_s = \int_{\Omega_s} I_\lambda(\vartheta)\,d\omega$$

The function $I_\lambda(\vartheta)/I_{\lambda 0}$ is shown in Figure 7: this Figure shows that the solar disk is more than a factor 2 fainter at the limb and a more than factor 1.2 brighter at the center with respect to the average disk intensity I_a. Given the average disk intensity I_a [W m^{-2} sr^{-1} nm^{-1}] this needs to be multiplied by the SPS responsivity $\varepsilon_{SPS}(\lambda)$ [Ampère/Watt] and integrated over all wavelengths and over the solid angle Ω_{SPS} subtended by the fraction of solar disk area seen in the penumbra where SPS are located in order to give the output current response R_{SPS} [A m^{-2}] by the SPS detectors

$$R_{SPS} = \int_{\Omega_{SPS}}\int_0^{+\infty} I_\lambda(\vartheta)\,\varepsilon_{SPS}(\lambda)\,d\lambda\,d\omega \qquad [\text{A m}^{-2}]$$

which is still depending on the SPS area. Now in order to compute R_{SPS} at least three different cases need to be considered:

1) the radiation emitted by the solar disk is uniformly distributed over the whole disk and equal to I_a,
2) the radiation emitted by the solar disk depends on the considered portion of the disk due to the limb darkening effect,
3) the radiation emitted by the solar disk depends on the considered portion of the disk due to the limb darkening and to the presence of a sunspot group located close to the limb.

In the first hypothesis is $I_\lambda(\theta) = I_a$ hence

$$R_{SPS} = \Omega_{SPS}\int_0^{+\infty} I_a\,\varepsilon_{SPS}(\lambda)\,d\lambda = f_{SPS}\int_0^{+\infty}\Omega_s I_a\,\varepsilon_{SPS}(\lambda)\,d\lambda = f_{SPS}\int_0^{+\infty} F_\lambda\,\varepsilon_{SPS}(\lambda)\,d\lambda \qquad [\text{A m}^{-2}]$$

where f_{SPS} is the fraction of the solar disk area seen by the SPS in the penumbra. Because the quantity f_{SPS} is computed geometrically as explained above and the integral is a constant (under the assumption of SPS responsivity constant ε_{SPS} with time), the above quantity can be computed by direct computation without any numerical integration. In particular, given the SPS responsivity curve shown in Figure 6, it turns out that $\int F_\lambda\,\varepsilon_\lambda\,d\lambda = 33.9619$ mA cm^{-2}. This value of the SPS output current results from a total irradiance (integrated over the 200-1100 nm wavelength interval of SPS responsivity curve) $\int F_\lambda\,d\lambda = 102$ mW cm^{-2} (to be compared with the quantity of about 137 mW cm^{-2} corresponding to the value of total irradiance integrated over the whole solar spectrum).

On the other hand, in the second hypothesis, both the integrations over different wavelengths and angular positions across the fraction of solar disk seen by the SPS need to be performed in order to compute the quantity

$$R_{SPS} = \int_{\Omega_{SPS}}\int_0^{+\infty} I_\lambda(\vartheta)\,\varepsilon_{SPS}(\lambda)\,d\lambda\,d\omega = \int_{\Omega_{SPS}}\int_0^{+\infty} I_{\lambda 0}\left(1 - u_\lambda - v_\lambda + u\cos\vartheta + v\cos^2\vartheta\right)\varepsilon_{SPS}(\lambda)\,d\lambda\,d\omega$$

Hence, numerical integration is needed in order to estimate the average solar radiation coming from the fraction of the disk seen by the SPS and taking into account the limb darkening. Under the simplifying assumption that the limb darkening coefficients u_λ and v_λ have a weak dependence on the wavelength over the SPS band-pass interval, hence constant values u_0 and v_0 can be assumed, the integrations over $d\lambda$ and $d\omega$ can be decoupled as follows

$$R_{SPS} = \int_{\Omega_{SPS}} \left(1 - u_0 - v_0 + u_0 \cos\vartheta + v_0 \cos^2\vartheta\right) d\omega \int_0^{+\infty} I_{\lambda 0}\, \varepsilon_{SPS}(\lambda) d\lambda = f_{SPS} \Omega_s \left\langle G(\vartheta) \right\rangle_{\Omega_{SPS}} \int_0^{+\infty} I_{\lambda 0}\, \varepsilon_{SPS}(\lambda) d\lambda$$

where the function $G(\vartheta) = 1 - u_0 - v_0 + u_0 \cos\vartheta + v_0 \cos^2\vartheta$ is averaged over the solid angle Ω_{SPS} subtended by the fraction of solar disk seen by the SPS. Because

$$F_\lambda = \int_{\Omega_s} I_{\lambda 0} G(\vartheta, \lambda) d\omega = I_{\lambda 0} \left\langle G(\vartheta, \lambda) \right\rangle_{\Omega_s} \Omega_s \quad \rightarrow \quad I_{\lambda 0} = \frac{F_\lambda}{\left\langle G(\vartheta, \lambda) \right\rangle_{\Omega_s} \Omega_s}$$

it turns out that the output SPS current response is

$$R_{SPS} = f_{SPS} \frac{\left\langle G(\vartheta) \right\rangle_{\Omega_{SPS}}}{\left\langle G(\vartheta) \right\rangle_{\Omega_s}} \int_0^{+\infty} F_\lambda \varepsilon_{SPS}(\lambda) d\lambda$$

The variations of the limb darkening coefficients over the SPS band-pass interval are shown in Figure 8, together with average values u_0 and v_0 estimated by averaging these coefficients over the SPS responsivity profile as $u_0 = \int u_\lambda\, \varepsilon_\lambda\, d\lambda / \int \varepsilon_\lambda\, d\lambda = 0.833458$ and $v_0 = \int v_\lambda\, \varepsilon_\lambda\, d\lambda / \int \varepsilon_\lambda\, d\lambda = -0.198740$. These values are shown as horizontal dotted and dashed lines in Figure 6 and will be assumed for the rest of the computation.

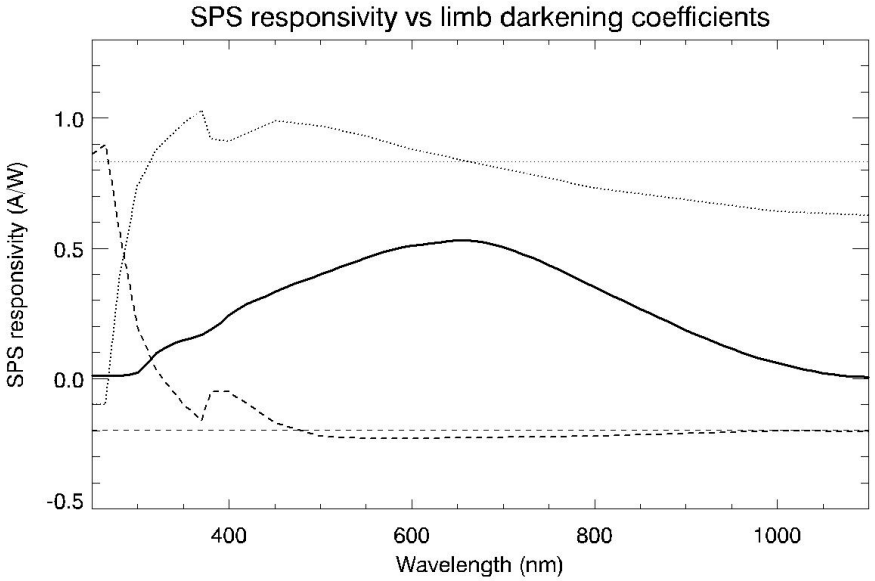

Figure 8: the SPS responsivity (solid line) and the variation as a function of wavelength of the limb darkening coefficients u_λ (dotted line) and v_λ (dashed line) as provided by [4].

We notice here that in general the variations of the limb darkening profile as a function of the wavelength are not negligible: for instance at the limb ($\vartheta = \pi/2$) we have $G(\vartheta)_{400\text{nm}} = 0.14$, $G(\vartheta)_{600\text{nm}} = 0.35$, $G(\vartheta)_{1000\text{nm}} = 0.56$. Possible uncertainties due to this approximation are discussed in paragraph (4.1).

Under the third hypothesis the above formulas are still valid, but the function $G(\vartheta)$ needs to be replaced by a different function $G_{spot}(\vartheta)$ providing the dimmed disk intensity at the location of the sunspot close to the limb. In this case the SPS output current response R_{SPS} [A m^{-2}] will be given by

$$R_{SPS} = f_{SPS} \frac{\left\langle G_{spot}(\vartheta) \right\rangle_{\Omega_{SPS}}}{\left\langle G(\vartheta) \right\rangle_{\Omega_s}} \int_0^{+\infty} F_\lambda \varepsilon_{SPS}(\lambda) d\lambda \quad [\text{A m}^{-2}].$$

3.2 Resulting SPS output response currents

The output response current R_{SPS} [A m^{-2}] expected by the SPS was computed in the penumbra around the location of SPS on the entrance pupil plane by assuming (as a first step) that the occulter and the coronagraph spacecraft are perfectly coaligned. The illumination in the penumbra has been computed for all the three cases mentioned above and resulting curves are shown in Figure 9. In general the inclusion of the limb darkening corresponds to a reduction by about a factor ~ 1.9 in the illumination level at the SPS location, while the presence of the sunspots induces a further decrease by about a factor ~ 1.1.

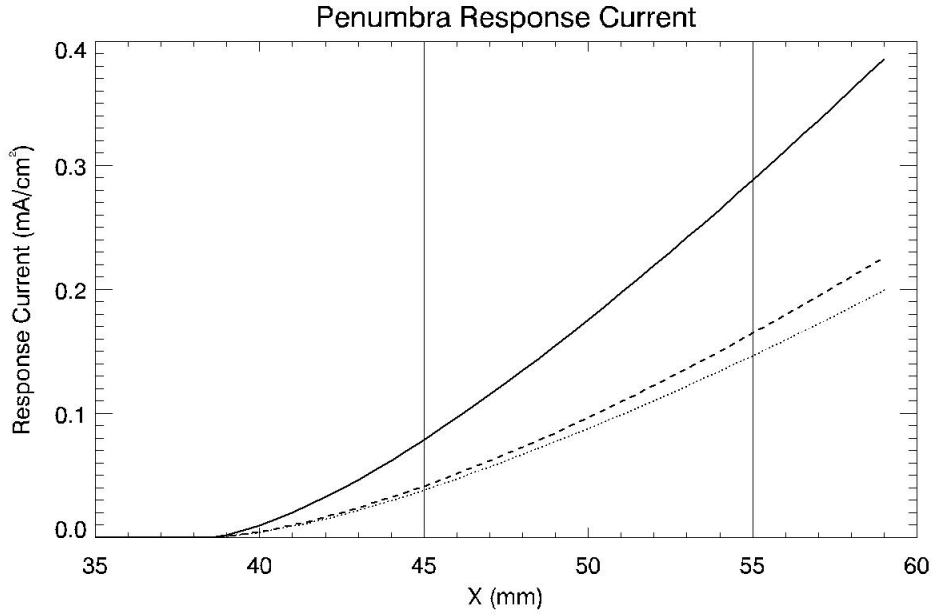

Figure 9: level of expected SPS response current in the penumbra on the entrance pupil plane as a function of the distance from the telescope optical axis around the SPS location radius at 55 mm (vertical solid line). The current is given for the three mentioned cases, i.e. by neglecting the limb darkening (solid line), including the limb darkening (dashed line) and adding to the limb darkening a sunspot located at the limb (dotted line).

The determination of the SPS response current curve when the limb darkening effect and a sunspot are also included requires a numerical integration of the limb darkening function given above and his modification due to the presence of a sunspot over the "crescent-shaped" fraction of solar disk "seen" by the considered point. To this end, each step of the computation needs the creation of 2D image representing the light distribution over the fraction of the solar disk "seen" by the considered point. Two examples are shown in Figure 10 for both cases of limb darkening without (left) and with (right) a sunspot at the limb: the computation was performed creating for every step of iteration a 1001x1001 pixels image as those shown in Figure 10. The sunspot was created by adding two concentric elliptical regions at the limb where the photospheric emission is reduced respectively by a factor 0.15 and 0.7 for the sunspot umbra and penumbra. The sunspot umbra and penumbra are assumed to have a circular shape with radii equal to $R_{umb} = 0.1\ R_{sun}$ and to $R_{pen} = 0.15\ R_{sun}$; the circular spot is then converted into an elliptical shaped spot by taking into account simple geometrical projection due to its location close to the limb and then was centered at the East limb $0.04\ R_{sun}$ inside the disk (see Figure 10). This significant size was selected in order to simulate the effect not of a single spot, but a big sunspot group; the effect of a much smaller sunspot (not shown in Figure 10) has been simulated as well, by assuming $R_{umb} = 0.05\ R_{sun}$ and $R_{pen} = 0.075\ R_{sun}$.

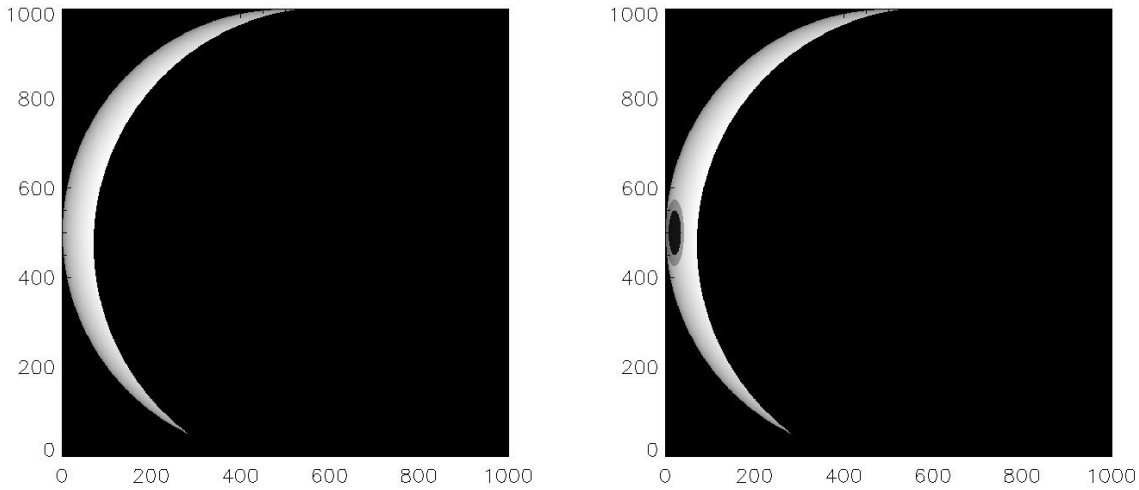

Figure 10: example of the light distribution over the fraction of solar disk emerging behind the occulter considering the presence of limb darkening (left) and by adding a sunspot at the East limb (right).

Given the response current curves shown in Figure 9, it is easy to estimate the expected change in the current level due to an occulter displacement in the x or y direction with respect to the current expected when the occulter and the coronagraph are perfectly aligned. These changes are shown in Figure 11 by assuming that the 8 SPS are located on a circumference with radius r_{SPS} = 55 mm from the optical axis.

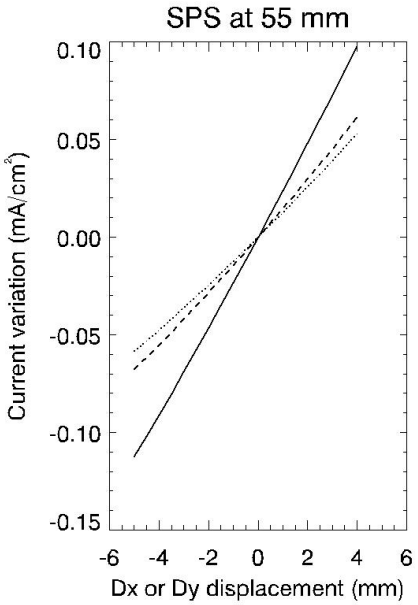

Figure 11: variation of the expected SPS response current as a function of the occulter displacement in the direction parallel to the entrance pupil plane for the three cases: no limb darkening (solid) line), limb darkening (dashed line) and limb darkening plus sunspot (dotted line). Current variations are shown for the SPS located at 55 mm from the optical axis.

More in general, the geometrical technique described so far can be used to determine the 2D distribution of the penumbral SPS current [mA cm^{-2}] for the general case of any given displacement of the occulter spacecraft in the

direction perpendicular (*x* and *y* coordinates) and parallel (*z* coordinate) to the telescope optical axis, taking also into account any possible angular tilt of the occulter. The resulting SPS 2D response current distributions are shown in Figure 12 for different cases (no limb darkening, limb darkening, and limb darkening plus sunspot).

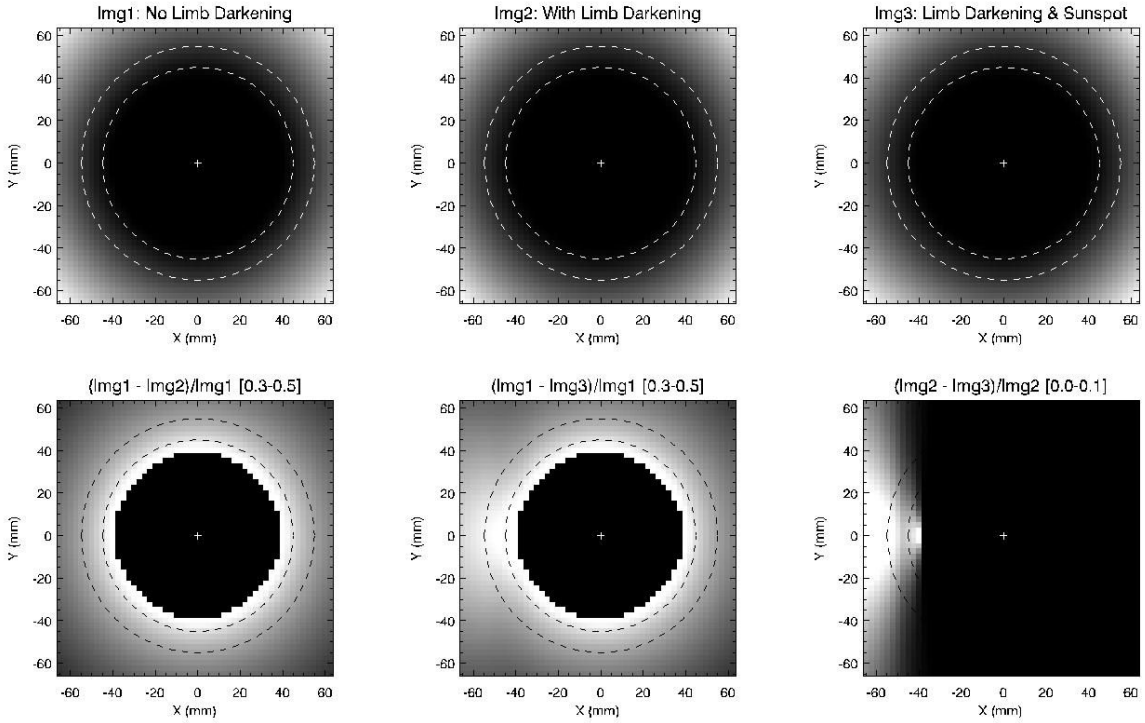

Figure 12, top: distribution of response currents [mA cm^{-2}] in the penumbra when the occulter is aligned with the spacecraft for the case without limb darkening (left), with limb darkening (middle) and with limb darkening plus a sunspot at the limb (right). Bottom: relative differences between the above images (see plot titles). In all plots the dashed circular lines shows the radius where SPS will be located at 55 mm from the optical axis and more internal circle at 45 mm.

Plots in Figure 12 show many important results. First: the decrease in the penumbral current distribution taking into account the limb darkening effect is not uniformly distributed, but is dependent on the considered distance from the optical axis, hence is dependent on the amount of displacement on the (x, y) plane. This can be understood as follows: because of the limb darkening the disk is darker closer to the limb and brighter moving away from the limb (Figure 7), hence for larger displacements the average illumination due to the fraction of visible disk increases, thus the SPS current. Hence, the difference with or without limb darkening is relatively larger for points located closer to the inner edge of the penumbra (Figure 12, bottom left panel). Second: the presence of the sunspot at the limb results in a further reduction of the average illumination in the penumbra all over the column of the image located above the location of the spot (Figure 12, bottom middle and right panel).

The illumination in the penumbra and then the response current can also be more nicely visualized as a 3D colored surface, shown in Figure 13. This Figure also suggests that the resulting 3D surface is quite similar to a rotational pseudo-paraboloid: this means that around the location of SPS it could be possible in principle to approximate the expected current with a pseudo-paraboloid fitting surface, as we discuss in paragraph (7).

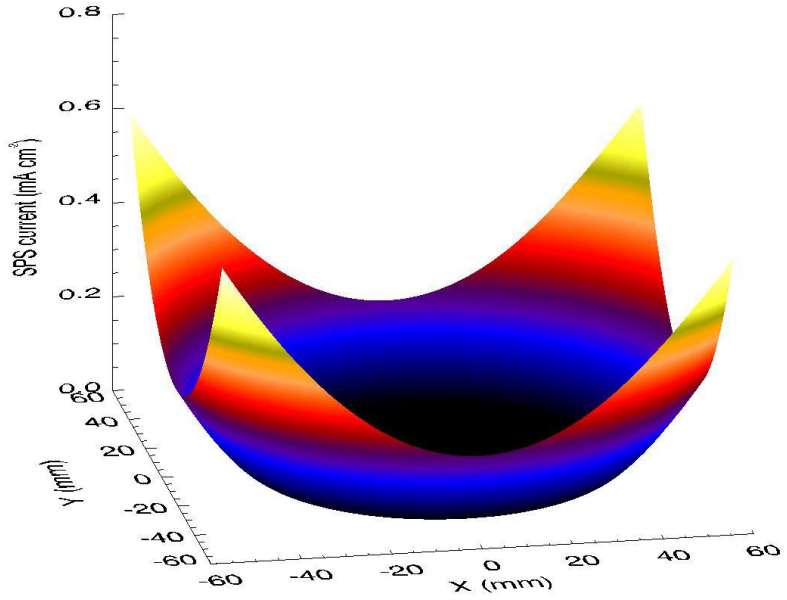

Figure 13: SPS response current in the penumbra (mA cm^{-2}) around the edge of the umbra where the SPS will be located.

4 CORRECTIONS TO THE COMPUTED IRRADIANCE CURVE

Because of some assumptions introduced in the above computations, it's necessary to introduce some corrections in the computed irradiance values in order to take into account for:

1. The approximation introduced with the weighted wavelength average of limb darkening factors u_0 and v_0;
2. The seasonal variations in the TSI value due to the changing Earth-Sun distance;
3. The physical spatial dimensions of the SPS.

The modifications introduced by the above contributions are discussed below. We notice here that the diffraction from the occulter has not been taken into account in this analysis; see [9] for a discussion on the effects of diffraction.

4.1 Limb darkening function approximation

As explained in the above Sections, in order to reduce the computational time, it was necessary to introduce an approximation in the computation of the irradiance curve, and in particular to assume constant values for the limb darkening parameters $u_0 = \int u_\lambda\, \varepsilon_\lambda\, d\lambda \,/\, \int \varepsilon_\lambda\, d\lambda = 0.833458$ and $v_0 = \int v_\lambda\, \varepsilon_\lambda\, d\lambda \,/\, \int \varepsilon_\lambda\, d\lambda = -0.198740$, where ε_λ is the SPS responsivity function and u_λ and v_λ are the limb darkening coefficients (Figure 8). In order to quantify the error introduced with this approximation, we computed the following two convolution integrals

$$I_A(\vartheta) = \int_0^{+\infty} I_{\lambda 0}\left(1 - u_\lambda - v_\lambda + u_\lambda \cos\vartheta + v_\lambda \cos^2\vartheta\right)\varepsilon_{SPS}(\lambda)\, d\lambda$$

$$I_B(\vartheta) = \left(1 - u_0 - v_0 + u_0 \cos\vartheta + v_0 \cos^2\vartheta\right)\int_0^{+\infty} I_{\lambda 0}\, \varepsilon_{SPS}(\lambda)\, d\lambda$$

over a single radial slice of the solar disk. Figure 14 shows a comparison between these two quantities, both as a function of the angle ϑ between the line of sight pointing at the disk center and the radial at considered point on the disk (so that $\vartheta = \pi/2$ corresponds to the solar limb).

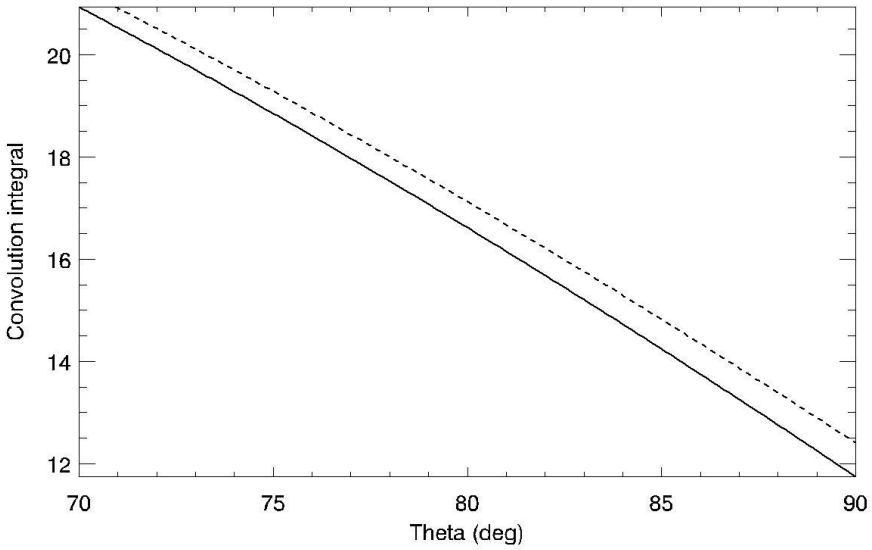

Figure 14: comparison between two convolution integrals I_A (solid line) and I_B (dashed line) showing the approximation introduced in the computation with the weighted average of limb darkening coefficients.

This Figure clearly shows that the two resulting curves are almost parallel, hence there are basically no corrections to be taken into account when one considers relative variations of the current. Moreover, the error introduced by this approximation can be corrected by introducing simply a constant multiplication factor K_λ. In particular, by averaging over the ϑ angle values shown in Figure 14 it turns out that the computed irradiances are slightly overestimated and that the correction factor is $K_\lambda = 0.980$.

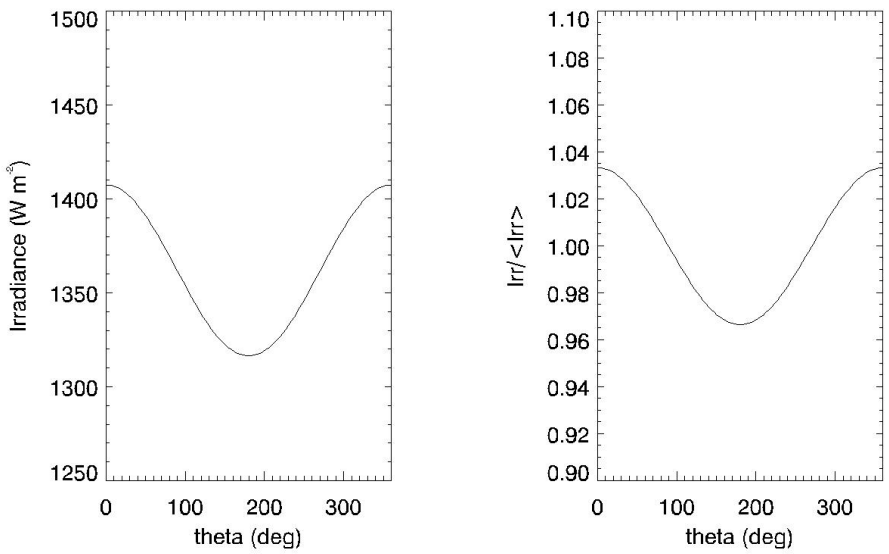

Figure 15: absolute (left) and relative (right) variations of the Total Solar Irradiance (TSI) during the period of 1 year as a function of the true anomaly angle measured along the Earth's orbit around the Sun.

4.2 Seasonal variations of total solar irradiance

Seasonal variations of the solar irradiance are simply due to variations of the Sun-Earth distance over a 1-year period, due to the eccentricity of the Earth's orbit; these variations are shown in Figure 15 over the period of one year. Irradiance values have been computed so far by assuming an average Sun-Earth distance corresponding to 1 AU = 149.5978707_x10^6 km. Taking into account the variation of the Sun-Earth distance it will be necessary to correct the irradiances by a yearly factor $K_Y(t)$ changing continuously with time t from a maximum value at perihelion K_Y = 1.0332 in early January to a minimum value at aphelion K_Y = 0.9664 in early July.

In summary, it is necessary to multiply the irradiance curves computed above by a correction factor given by $K_\lambda K_Y(t)$, with the values given above for K_λ and $K_Y(t)$.

4.3 Smoothing effect due to the SPS physical dimensions

Due to the physical dimension of the SPS the output current curve will have a different shape with respect to the original irradiance curve. In particular, the net effect will be a smoothing of the irradiance curve over the 2D area covered by the SPS. The resulting effective curve is shown in Figure 16, by assuming for instance an SPS side by 3mm: the most significant differences are present close to the edge of the penumbra, where the most significant variations in the slope of the curve are present, while at larger distances from the optical axis the irradiance curve becomes more similar to a straight line, thus making the effect of the SPS smoothing much smaller.

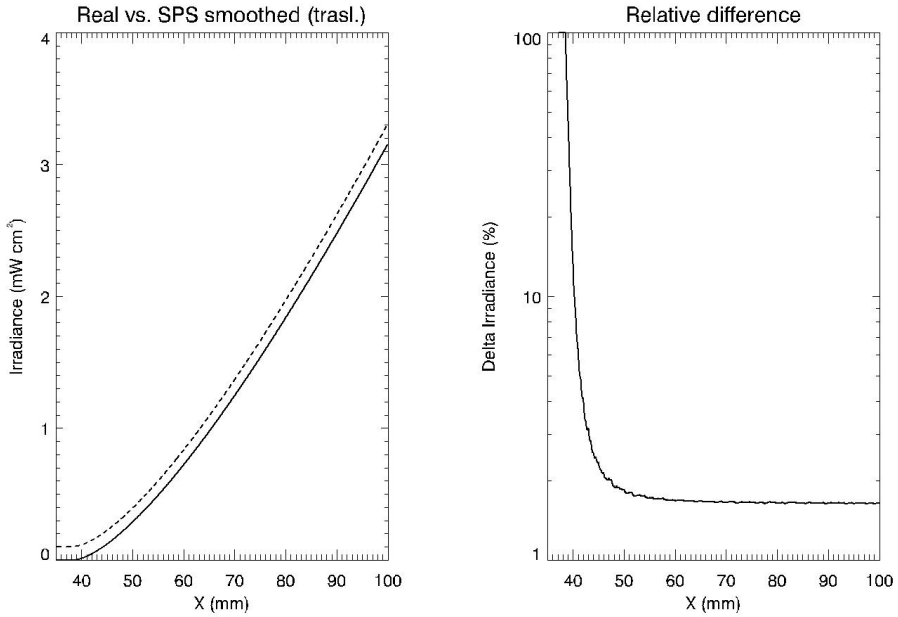

Figure 16, left: comparison between the original irradiance curve (solid) and the effective curve obtained by averaging over the spatial dimension of the SPS (dashed, translated by 0.1 mW cm^{-2}). Right: relative difference between the two curves shown in the left plot.

5 NUMERICAL TESTS ON THE PENUMBRA ILLUMINATION CURVE

5.1 Test on the effect of sunspots based on real data

As mentioned above the presence of solar sunspots at the limb will modify the level of illumination in the penumbra by an amount comparable with the sensitivity required to perform the SPS measurements. In particular, as solar sunspots will be dragged by the solar rotation in the visible hemisphere, the modification in the resulting penumbra illumination curve will evolve in time.

To this end, we downloaded a sequence of SDO/HMI full disk images acquired between October 17-18 2014, in a time period when a big sunspot group (NOAA 12192) is appearing on the visible hemisphere at the West limb dragged by the solar rotation. The image sequence has been used to reconstruct the simulated penumbra illumination profile during the selected observational period: results are shown in Figure 17. In particular in this Figure images in the left column show the difference in the penumbra illumination profile with respect to the first frame we analyzed corresponding to a time before the appearing of the sunspot, while images in the right column provide the corresponding disk image. It turns out that during the appearance of the sunspot the whole penumbral region located in the area above the tangent at the disk at the sunspot latitude will be affected by a decrease in the illumination level by up to 3%. During the solar rotation the affected area will first appear closer to the umbra edge, and then will propagate outward as the sunspot will move farther from the limb.

This test with real data demonstrate that when significant sunspots will appear on disk, the modification in the penumbra illumination curve will be larger than the sensitivity required to measure the minimum tangential displacement of one spacecraft with respect to the other one.

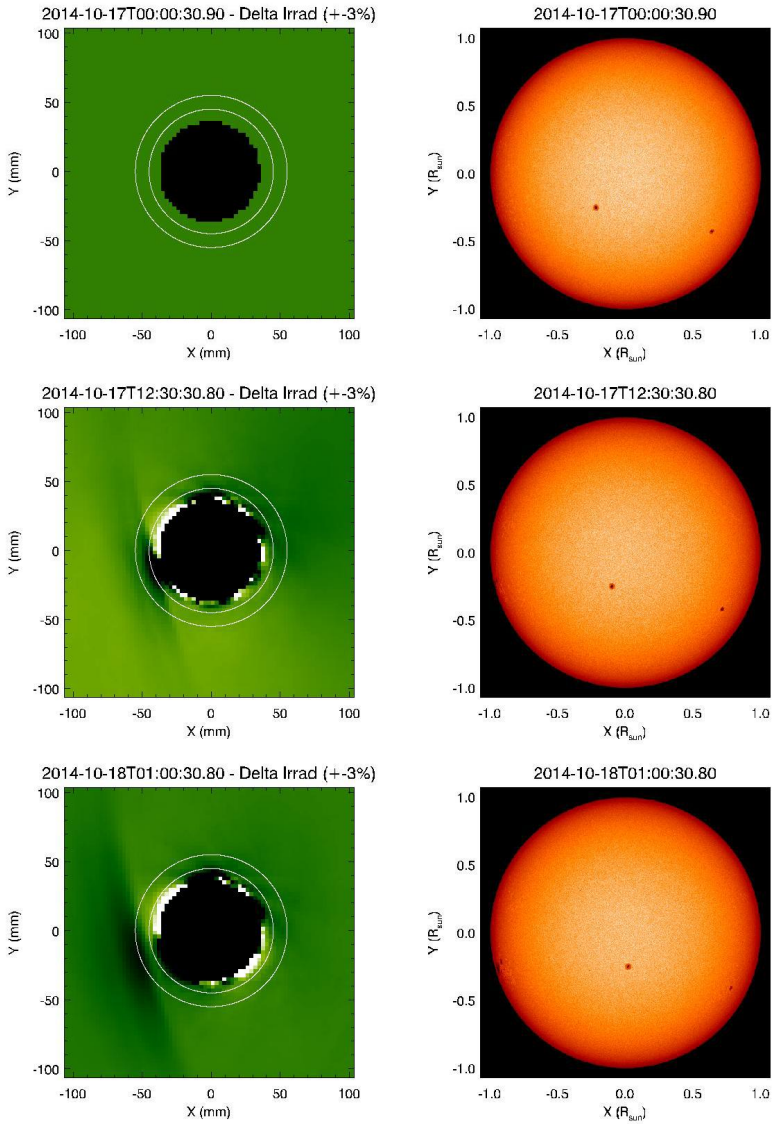

Figure 17: relative variation (left column, color scale ±3%) of the penumbra illumination profile with respect to the no-sunspot case during the appearance of a sunspot at the West limb dragged by solar rotation (right column).

5.2 Test with an oversimplified penumbra illumination curve

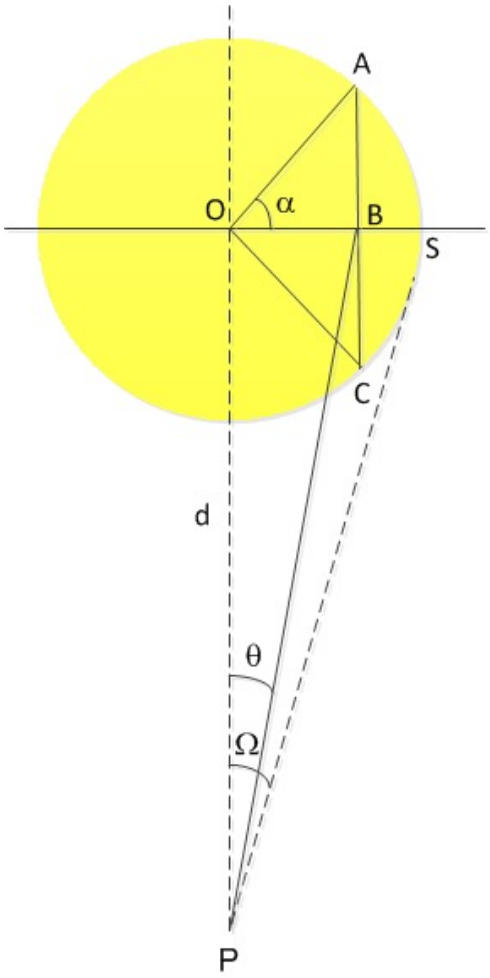

Figure 18: simplified computation of the penumbra illumination profile (see text).

In order to verify the correctness of the penumbra illumination profile we describe here a numerical test we performed by assuming that the area of Sun seen in the penumbra can be approximated with the area of the sector ABCS (Figure 18). It can be shown that this area is linked to the angle α by the relation:

$$A_{ABCS} = \frac{1}{2} R_{Sun}[2\alpha - \sin(2\alpha)]$$

The irradiance at the point P is proportional to the area ABCS. The angle α is linked to the angle θ by trigonometric relations $OB = d\tan(\theta) = OA\cos(\alpha)$. Solving the equivalence, we have

$$\alpha = \cos^{-1}\left(\frac{d\tan(\theta)}{OA}\right) = \cos^{-1}\left(\frac{\tan(\theta)}{\tan(\Omega)}\right)$$

The flux at on the entrance pupil plane is proportional to the area of the crescent Sun multiplied by the corresponding value of the limb darkening, under the oversimplifying assumption to have the limb darkening constant over the whole

considered Sun area. This hypothesis is provides a good approximation as far as the considered crescent area is small, hence only for point in the penumbra being located closer to the edge of the umbra.

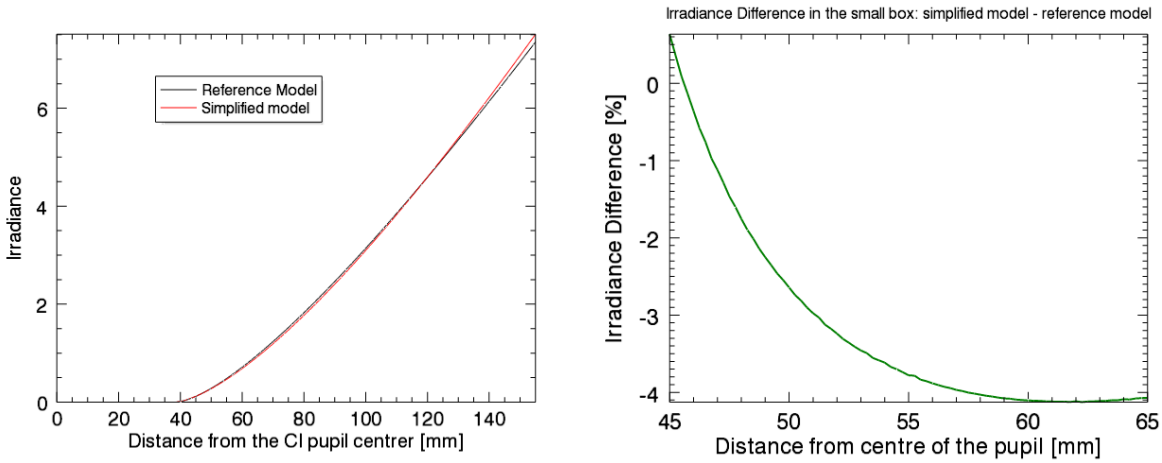

Figure 19: comparison between the reference and the simplified penumbra illumination profiles (left) and the relative difference between the two profiles (right).

The resulting penumbra illumination profile is shown in Figure 19, normalized to the reference illumination profile derived with the more complex procedure described in previous paragraphs. Comparison in this Figure shows that at the distance from the optical axis where the SPS will be located (55 mm) the difference between the two models is significant, much larger than the sensitivity required to provide the absolute FF metrology.

6 SPS REQUIRED SENSITIVITIES AND DYNAMIC RANGES

Once the 2D distribution of the SPS response currents have been estimated, it is possible to use these values to estimate the sensitivities required to detect the occulter displacements in agreement with performance requirements，i.e. “a lateral measurement accuracy of 50μm (3-σ) in each axis, and a longitudinal measurement accuracy of 1 mm (3-σ)”. The required sensitivities have been then computed as the relative difference in the response current curve once a minimum displacement by 50μm and by 1 mm occurs along the X and Z axes, respectively. Resulting required sensitivities for lateral and longitudinal displacements are shown in Figure 20 and Figure 21, respectively.

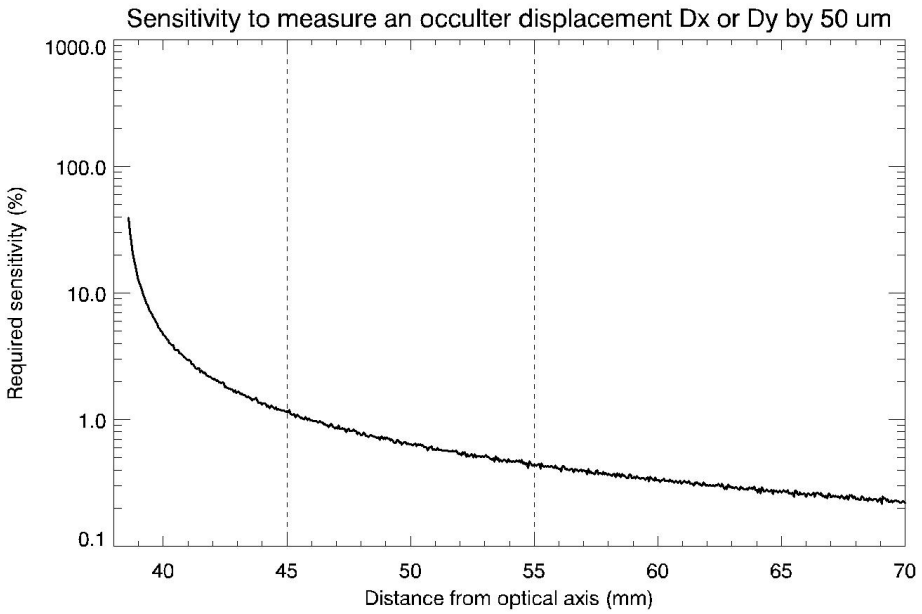

Figure 20: SPS currents required sensitivity to detect the minimum lateral displacement of 50μm as a function of the distance from the optical axis measured on the entrance pupil plane.

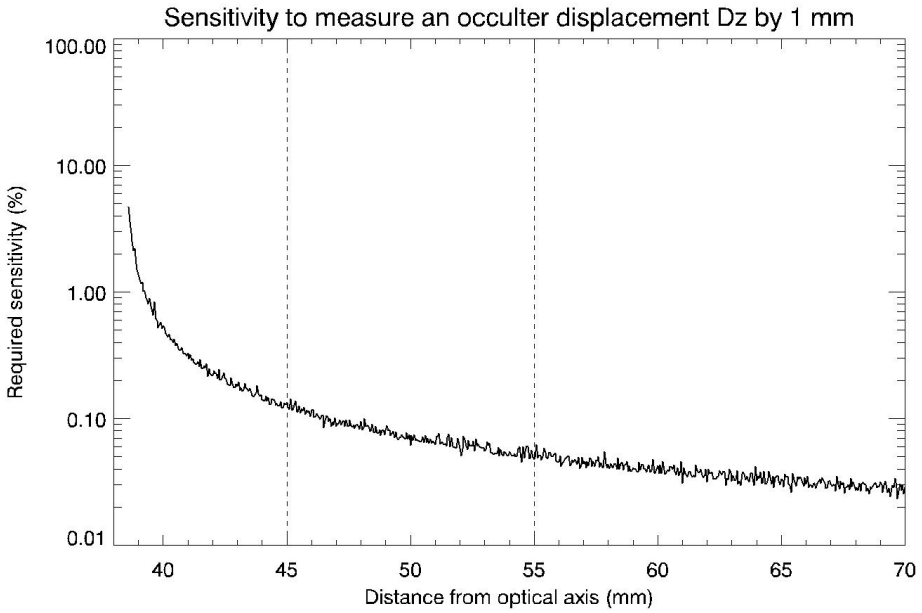

Figure 21: SPS currents required sensitivity to detect the minimum longitudinal displacement of 1 mm as a function of the distance from the optical axis measured on the entrance pupil plane.

These Figures clearly demonstrate that with actual position of SPSs at 55 mm:

- the required sensitivities to detect the minimum lateral displacement in agreement with performance requirements is 0.45% ~ 0.5% with SPSs at 55 mm (the minimum required sensitivity decreases going farther from the optical axis because the slope of the current curve increases much slower than the absolute value of the current to measure);
- the required sensitivity to detect the minimum longitudinal displacement in agreement with performance requirements is 0.048% ~ 0.05% for SPSs at 55 mm.

Hence, the above values show that the requirement of longitudinal displacement is more challenging than the requirement for lateral displacement. As for the SPS performance goal "SPS should be able to return a 3D relative position measurement at reduced performance within a range of ±50 mm in lateral and ±500 mm in longitudinal": the SPS required dynamic range has been estimated by computing (with low spatial resolution, to save computational time) 2D maps of SPS currents for a large number of longitudinal displacements of the occulter covering the required range by ±500 mm.

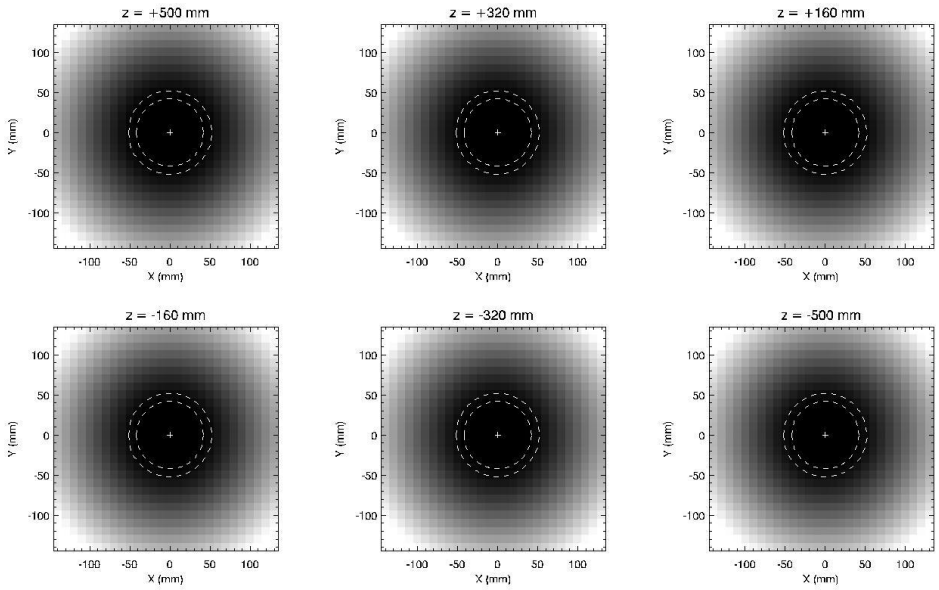

Figure 22: distribution of output SPS currents on the entrance pupil plane for different longitudinal displacements of the occulter (Z coordinate in the plot titles); the linear color scale is the same for all the plots.

Figure 22 shows the resulting 2D distributions of SPS output currents for different occulter longitudinal displacements: this Figure (where all values are plotted with the same linear scale) clearly shows that the expected current variations for longitudinal displacements will be quite small. In order to better quantify this small variation, horizontal cuts of the current expected along the X axis for different occulter longitudinal displacements are shown in Figure 23.

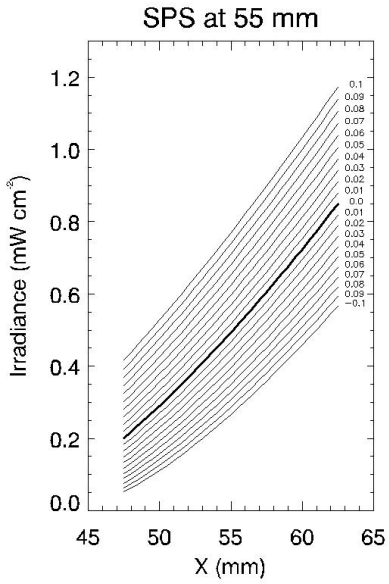

Figure 23: distribution of the irradiance around the position of the SPS at 55 mm at the reference position of the two spacecraft (thick line) and for positive (ISD increase) and negative (ISD decrease) displacements of the occulter along the z-axis as indicated by the reference numbers in the plots (given in units of m).

The overall dynamic range in the output currents has been derived by computing the expected response currents for the larger lateral and longitudinal displacements to be considered according to the performance goal.

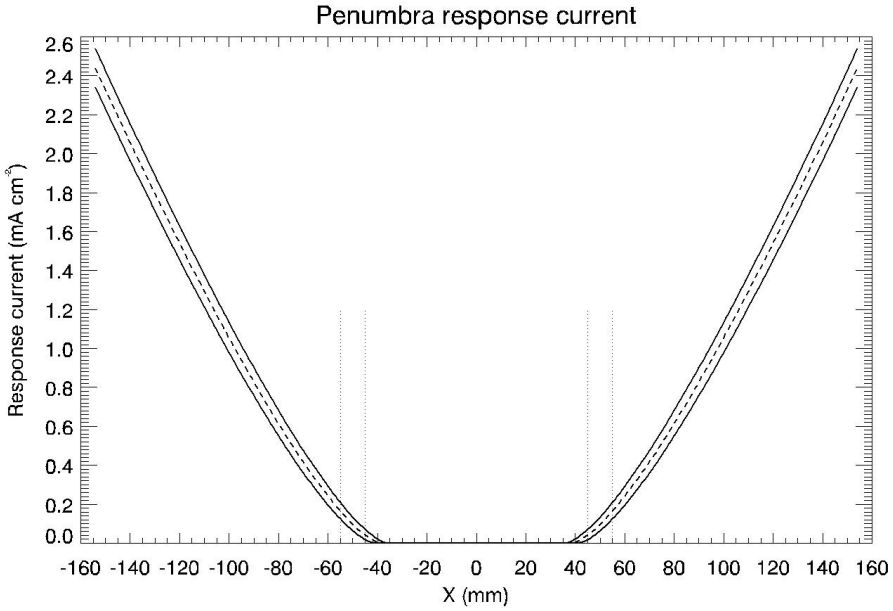

Figure 24: expected variation of the output SPSs currents for large lateral displacements (x-axis) for zero longitudinal occulter displacement (dashed line) and maximum / minimum longitudinal occulter displacements by ±500mm (solid lines).

The resulting output current curves are shown in Figure 24. This Figure leads to conclude that the expected output current in the corner of the outer SPSs in the goal box range ($55+50\cdot\sqrt{2}$mm = 125.71 mm) will be 1.6800 mA/cm^2, and that a longitudinal displacement of the occulter spacecraft by +500mm (i.e. towards the telescope spacecraft) or by -500mm (i.e. away from the telescope spacecraft) will change this current to values of 1.5918 mA/cm^2 and 1.7701 mA/cm^2 respectively; hence the latter value corresponds to the maximum current expected from the SPS in the goal box. On the

other hand, in the corner of the smallest requirement box range (55+10·√2mm = 69.14 mm) the expected output current will be 0.4009 mA/cm^2, and a longitudinal displacement of the occulter spacecraft by +100mm (i.e. towards the telescope spacecraft) or by -100mm (i.e. away from the telescope spacecraft) will change this current to values of 0.3896 mA/cm^2 and 0.4124 mA/cm^2 respectively; hence the latter value corresponds to the maximum current expected from the SPS in the requirement box.

On the other hand, the minimum current to be measured will be close to 0 or to the sum of different sources of noise, as it happens when in the goal box range one of the SPSs will entirely fall in the umbral region (neglecting stray light). In the smaller requirement box if we assume as minimum value the current expected on the SPS at 55mm for a tangential displacement by 10·√2 mm towards the edge of the umbra (hence at 55 – 14.14 = 40.86 mm) and for a longitudinal displacement by +100mm towards the telescope spacecraft, then this value will correspond to 6.273·10^{-3} mA/cm^2.

Consequences of the above values on the SPS electronic design are discussed in [10].

7 PRELIMINARY SPS ALGORITHM

The determination of an algorithm able to provide the position of the occulter (hence values of coordinates x_0, y_0, z_0 of the occulter center and its tilt angle ϑ) given measured requires the determination of a function F relating the signal s_i measured at the location (x_i, y_i, z_i) of the SPS and the solution of a system of four equations with four unknown quantities (x_0, y_0, z_0, ϑ) so that

$$s_i = F(x_i, y_i, z_i, x_0, y_0, z_0, \vartheta),\ i = 1, 2, 3, 4 \quad \leftrightarrow \quad (x_0, y_0, z_0, \vartheta) = G(s_i, x_i, y_i, z_i),\ i = 1, 2, 3, 4$$

Nevertheless, to write all together the previous equations with a single explicit function F and derive the explicit expression for the inverse function G is – if possible – a quite complicate task, as we showed in paragraph (8).

A possible alternative solution is to derive a simple fitting function F' for the irradiance surface or the output current surface F (Figure 13), and the simplest attempt is to try to fit this function with a 2D pseudo-paraboloid. We started with the simplest case of polynomial fittings of the one-dimensional curve corresponding to the radiance plotted along the x direction around the location of SPS.

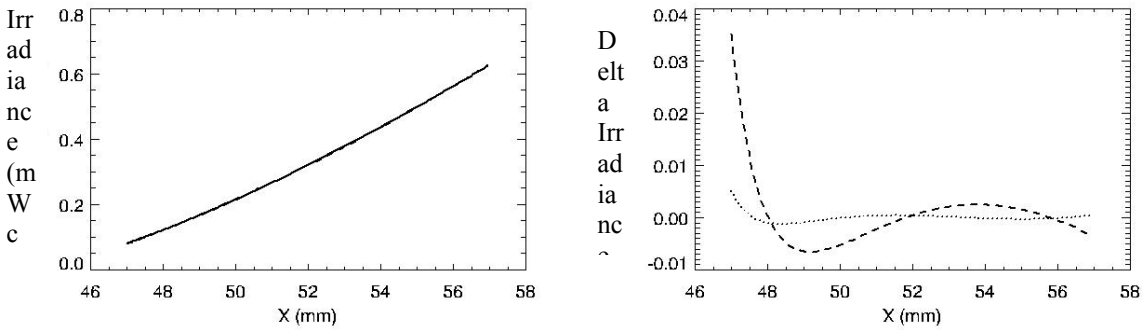

Figure 25, left: radiance curve (mWatt cm^{-2}) plotted along the x-axis around the location of SPS at 52 mm from the center of the optical axis (second and third order polynomial fitting are also overplotted). Right: relative differences between the radiance curve shown on left and the second (dashes) and third (dotted) order polynomial fitting curves.

As shown in Figure 25, by considering a range around the location of SPS at 55 mm, a second order polynomial fitting is able to reproduce the irradiance curve with an error smaller than 3.5%, while with the third order polynomial fitting the maximum error reduces to 0.5%. Hence, a second order paraboloid is not appropriate to approximate the shape of the irradiance distribution, because the errors induced by the fit will be larger than the minimum variation in the signal expected for the minimum lateral displacement by 50μm.

Hence, we assumed that around the location of SPS the irradiance curve $R(x,y)$ shown in Figure 25 can be well approximated with the equation of a Nth-order pseudo-paraboloid centered at the point (x_0, y_0). In general, an elliptical pseudo-paraboloid of degree N can be written as

$$R = R_0 + \sum_{n=1}^{N} \frac{|x - x_0|^n}{a_n^n} + \frac{|y - y_0|^n}{b_n^n}$$

with $a_n \neq b_n$ coefficients providing the oblateness of the paraboloid on the (x,y) plane. The first step forward with respect to the second-order paraboloid, is to consider a third-order pseudo-paraboloid by assuming no tilt ($\vartheta = 0$) of the occulter (hence $a_n = b_n$), which is given by

$$R = R_0 + \frac{|x - x_0| + |y - y_0|}{a} + \frac{(x - x_0)^2 + (y - y_0)^2}{b^2} + \frac{|x - x_0|^3 + |y - y_0|^3}{c^3}$$

for a circular pseudo-paraboloid with axis of symmetry parallel to the z-axis, vertex located in the point (x_0, y_0, R_0). In the above expression the x and y (cm) variables measure the coordinates of the occulter center projected on the entrance pupil plane, while R_0 (mW cm^{-2}) represents the irradiance at the vertex of the paraboloid.

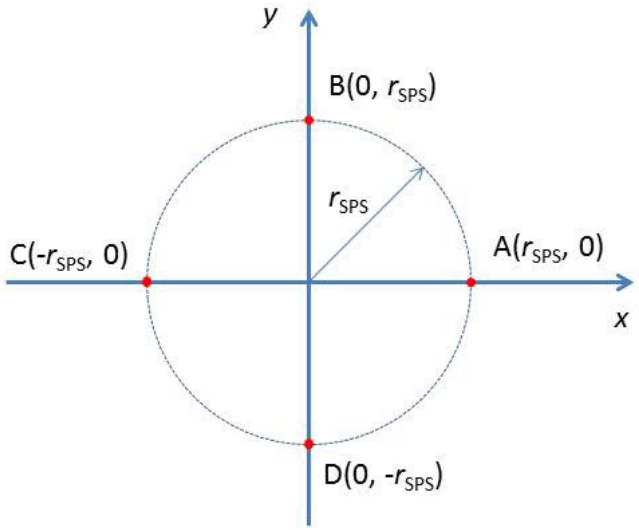

Figure 26: *location of the four SPS with respect to the reference system.*

Now, if we consider 4 SPS located in the points A, B, C and D shown in Figure 26, it is possible to show that, given the measurements of irradiance R_A, R_B, R_C, R_D in this four points, then (as far as $x_0, y_0 < r_{SPS}$ hence $|r_{SPS} - x_0| = r_{SPS} - x_0$ and $|r_{SPS} - y_0| = r_{SPS} - y_0$) the coordinates of the pseudo-paraboloid vertex (x_0, y_0) are given by the solutions of the following equations:

$$\begin{cases} x_0^3 + c^3\left(\frac{1}{a} + \frac{2r_{SPS}}{b^2} + \frac{3r_{SPS}^2}{c^3}\right)x_0 + (R_A - R_C)\frac{c^3}{2} = 0 \\ y_0^3 + c^3\left(\frac{1}{a} + \frac{2r_{SPS}}{b^2} + \frac{3r_{SPS}^2}{c^3}\right)y_0 + (R_B - R_D)\frac{c^3}{2} = 0 \end{cases}$$

where the (x_0, y_0) coordinates corresponds directly to the location of the occulter center on the (x, y) plane. The above cubic algebraic equations for x_0 and y_0 have similar coefficients, and can be both rewritten as

$$v^3 + Av + \Delta R = 0$$

$$A = c^3\left(\frac{1}{a} + \frac{2r_{SPS}}{b^2} + \frac{3r_{SPS}^2}{c^3}\right); \Delta R = \begin{cases} (R_A - R_C)\dfrac{c^3}{2}, v = x_0 \\ (R_B - R_D)\dfrac{c^3}{2}, v = y_0 \end{cases}.$$

The 3 roots (in general on the complex plane) of the above third-order equation are then given by

$$v_1 = 2\sqrt{-A/3}\cos\left[\frac{1}{3}\cos^{-1}\left(\frac{-\Delta R}{2\sqrt{-(A/3)^3}}\right)\right]$$

$$v_2 = 2\sqrt{-A/3}\cos\left\{\frac{1}{3}\left[\cos^{-1}\left(\frac{-\Delta R}{2\sqrt{-(A/3)^3}}\right) + 2\pi\right]\right\}$$

$$v_3 = 2\sqrt{-A/3}\cos\left\{\frac{1}{3}\left[\cos^{-1}\left(\frac{-\Delta R}{2\sqrt{-(A/3)^3}}\right) + 4\pi\right]\right\}$$

Between the above 3 solutions, only the last one v_3 has the property that $v_3 = 0$ when $\Delta R = 0$, as it happens when the pseudo-paraboloid is centered in (x_0, y_0). Hence the last one is considered to be the only real solution for (x_0, y_0), which are thus given by:

$$\begin{cases} x_0 = 2\sqrt{-A/3}\cos\left\{\dfrac{1}{3}\left[\cos^{-1}\left(\dfrac{(R_C - R_A)c^3}{4\sqrt{-(A/3)^3}}\right) + 4\pi\right]\right\} \\ y_0 = 2\sqrt{-A/3}\cos\left\{\dfrac{1}{3}\left[\cos^{-1}\left(\dfrac{(R_D - R_B)c^3}{4\sqrt{-(A/3)^3}}\right) + 4\pi\right]\right\} \end{cases}.$$

The above formula provides the absolute measurements for the pseudo-paraboloid vertex (x_0, y_0) corresponding to the center of the penumbra distribution, hence to the projected location of the occulter. On the other hand, the R_0 variable is related with the location z_0 of the occulter center along the z axis (as explained below) and can be derived independently from any of the 4 radiance values R_A, R_B, R_C, R_D as:

$$\begin{cases} R_{0A} = R_A - \dfrac{(r_{SPS} - x_0) + y_0}{a} - \dfrac{(r_{SPS} - x_0)^2 + y_0^2}{b^2} - \dfrac{(r_{SPS} - x_0)^3 + y_0^3}{c^3} \\ R_{0B} = R_B - \dfrac{x_0 + (r_{SPS} - y_0)}{a} - \dfrac{x_0^2 + (r_{SPS} - y_0)^2}{b^2} - \dfrac{x_0^3 + (r_{SPS} - y_0)^3}{c^3} \\ R_{0C} = R_C - \dfrac{(r_{SPS} + x_0) + y_0}{a} - \dfrac{(r_{SPS} + x_0)^2 + y_0^2}{b^2} - \dfrac{(r_{SPS} + x_0)^3 + y_0^3}{c^3} \\ R_{0D} = R_D - \dfrac{x_0 + (r_{SPS} + y_0)}{a} - \dfrac{x_0^2 + (r_{SPS} + y_0)^2}{b^2} - \dfrac{x_0^3 + (r_{SPS} + y_0)^3}{c^3} \end{cases}$$

$$\Rightarrow R_0 = \frac{1}{4}(R_{0A} + R_{0B} + R_{0C} + R_{0D})$$

The final value of R_0 will be then given by the average of the above 4 independent measurements. For the general determination of the z_0 coordinate, we have to consider that a variation of the ISD due for instance to a translation along Z of the occulter will result in first approximation in a vertical translation of the paraboloid representing the 2D distribution of irradiance on the entrance pupil plane, as it is shown in Figure 23. As a consequence, there is a direct relationship between the irradiance at the vertex R_0 of the fitting pseudo-paraboloid and the z_0 coordinate, as it is shown in Figure 27. In particular the curve shown in Figure 27 relating z_0 and R_0 can be well approximated with a linear fitting, hence given R_0 value the z_0 coordinate will be provided by:

$$z_0 = K + H\,R_0$$

with K and H constant values derived with the linear fit.

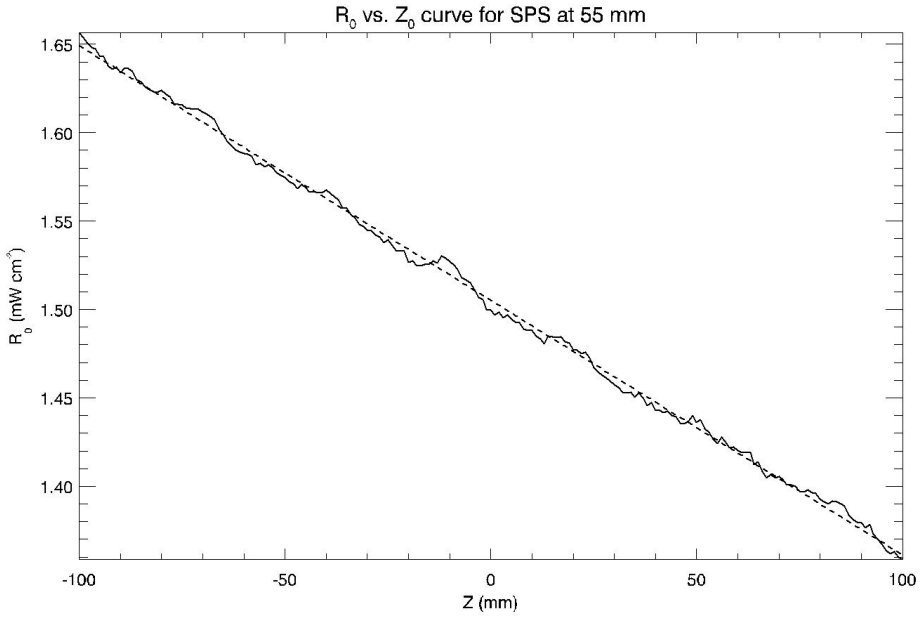

Figure 27: variation of the irradiance R0 at the pseudo-paraboloid vertex as a function of the ISD value z0.

Notice here that in the above algorithm example the quantity r_{SPS} will be fixed by the system geometry and the parameters reconfigurable from the ground will be: a, b, c, K and H.

8 SUMMARY AND CONCLUSIONS

In this paper we summarized all the main ingredients required to provide reliable measurement techniques for the PROBA-3 Formation Flying (FF) metrology system based on the measurement with the Shadow Positioning Sensors (SPS) of the illumination level on the Coronagraph Spacecraft (CSC) entrance pupil plane due to the occulter being located on the Occulter Spacecraft (OSC). Given the required precisions in the absolute positioning measurements (a lateral measurement accuracy of 50μm, and a longitudinal measurement accuracy of 1 mm) the penumbra illumination level have to be known with a very high accuracy (on the order of 0.5% and 0.05% for the minimum lateral and longitudinal displacement, respectively). Hence, in the determination of the theoretical illumination profile it is mandatory to include many other effects not considered before, such as: the (wavelength dependent) limb darkening function, possible modification induced by the transit of sunspots, and seasonal variations due to the eccentricity of the Earth orbit. All these effects have been considered and described in this paper.

The resulting theoretical penumbra illumination curve is not a simple analytic function that can be inverted in order to provide an expression for the coordinates (x, y, z) of the OSC with respect to the CSC. Hence, the definition of an algorithm to perform the metrology measurements required the determination of a function able to reproduce the distribution of the illumination level with very high accuracy. In particular, the penumbra illumination has been fitted with a third-order pseudo-paraboloid and the resulting equations relating the measured illumination with the position of the considered point have been inverted, providing explicit expression for the future PROBA-3 absolute metrology algorithm.

REFERENCES

[1] Renotte E. et al., "ASPIICS: an externally occulted coronagraph for PROBA-3. Design evolution", Proc. of SPIE Vol. 9143, 91432M, (2014).

[2] Renotte E. et al., "Design status of ASPIICS, an externally occulted coronagraph for PROBA3", Proc. of SPIE, (2015).

[3] Loreggia, D. et al., “OPSE metrology system onboard of the PROBA3 mission of ESA”, Proc. of SPIE, (2015).

[4] Cox, A. N., “Allen's astrophysical quantities”, AIP Press; Springer, Edited by Arthur N. Cox., (2000)

[5] Borrero, J. M., & Ichimoto, K., “Magnetic Structure of Sunspots”, Living Reviews in Solar Physics, vol. 8, no. 4, (2011)

[6] Vivès, S. et al., “In-flight Validation of the Formation Flying Technologies using the ASPIICS/PROBA-3 giant coronagraph”, Proc. of SPIE Vol. 7010, 70103R, (2010).

[7] Stathopoulos, F. et al., “Simulation of the metrology of the PROBA-3/ASPIICS formation flying solar coronagrah”, Proc. of SPIE Vol. 7731, 773144, (2010).

[8] Vivès, S. et al., “Demonstrator of the formation flying solar coronagraph ASPIICS/PROBA-3”, Proc. of SPIE Vol. 7731, 773147, (2010).

[9] Landini F., Bemporad A., Focardi M. et al., “Significance of the occulter diffraction for the PROBA3/ASPIICS formation flight metrology”, Proc. of SPIE, (2015).

[10] Focardi, M., et al., “Formation Flying Metrology for the ESA-PROBA3 Mission: The Shadow Position Sensors (SPS) silicon photomultipliers (SiPMs) readout electronics”, Proc. of SPIE, (2015).